

Journal of
Applied Remote Sensing

**Analysis of surface radiation
budget during the summer and
winter in the metropolitan area
of Beijing, China**

Ji Zhou
Deyong Hu
Qihao Weng

Analysis of surface radiation budget during the summer and winter in the metropolitan area of Beijing, China

Ji Zhou,^a Deyong Hu,^{b, c} and Qihao Weng^d

^a Beijing Normal University, College of Resources Science and Technology, State Key Laboratory of Earth Surface Processes and Resource Ecology, 100875 Beijing, China
zhouji@ires.cn

^b Capital Normal University, College of Resources Environment and Tourism, 100048 Beijing, China

^c Beijing Normal University and Institute of Remote Sensing Applications of Chinese Academy of Sciences, State Key Laboratory for Remote Sensing Science, 100101 Beijing, China

deyonghu@163.com

^d Indiana State University, Department of Geography, Center for Urban and Environmental Change, 47809 Terra Haute, USA
qhweng@gmail.com

Abstract. Estimation of surface radiation budget is a crucial step to analyze the climate effects caused by rapid urbanization. This paper reports a study of the integration of remote sensing images and ancillary data for analyzing the spatial and temporal variations of surface radiation budget in Beijing, China. Landsat-5 Thematic Mapper (TM) images and meteorological data of Beijing metropolitan area acquired in the summer and winter were used to calculate land surface parameters and surface radiation fluxes, including shortwave net radiation, effective radiation and net radiation. Validation with *in situ* measurements shows that the calculation of net radiation yielded high accuracy. It suggests that the integration of remote sensing and ancillary data provide an applicable and feasible routine for analysis of surface radiation budget in urban environment. In order to understand the spatial patterns of surface radiation budgets, parameters, such as radiation fluxes, albedo and land surface temperature, were analyzed in terms of variations among different land cover types. Results indicate that the city can be characterized as a “basin” of net radiation in the summer, while it is characterized as a “plateau” in the winter. The albedo and land surface temperature were two primary factors contributing to the spatial variations of net radiation, while the solar elevation angle controlled the seasonal variations of the absolute amount.

Keywords: surface radiation budget, Landsat TM, urban, Beijing.

1 INTRODUCTION

It has been demonstrated that urbanization induces adverse climatic effects. At the macro-scale, urbanization is one of the most important driving forces for global climate change [1]; while at the local scale, it creates urban climatic effects, such as urban heat islands (UHIs), air pollution, and so on, affecting energy consumption and the life quality of urban residents. As the dominant element of energy exchange between land surface and atmosphere, surface radiation budget is a key parameter for the climate and its changes. Surface radiation budget, which is also named as net radiation or radiation balance, is defined as the difference between the incoming and outgoing radiation fluxes including both longwave and shortwave radiation at the ground [2]. Because of intense human activities and complicated artificial landscapes, the surface radiation budget in urban environment is different from that of natural surfaces,

such as forest, agriculture land, and so on. Surface radiation budget is one of the focuses but major challenges to study the energy exchange processes between land surface and atmosphere in the urban areas, and this issue is especially crucial for mega-cities.

As a matter of fact, natural surfaces at different scales are the primary targets for surface radiation budget studies based on remote sensing models [3-6]. However, limited researches about the surface radiation budget in the urban environment have been reported, because of the complexity of urban land surfaces and difficulty in radiation fluxes measurements acquisition. The traditional method to investigate this problem is by using *in situ* measurements, obtaining each component of the radiation balance equation, and then examining the diurnal and/or seasonal variations of surface radiation budget [7-12]. With the advent of satellite remote sensing, especially the remote sensors with higher spatial resolution at thermal channels, e. g. Landsat TM/ETM+, Terra ASTER, some researchers have examined the applicability and feasibility of these images to investigate the surface radiation budget in the urban and suburban areas [13-15]. It has been confirmed that the integration of remote sensing images and ancillary data is an appropriate and helpful route to grasp the patterns of surface radiation budget in different urban areas and at different spatial and temporal scales. Nevertheless, the estimation accuracy of the net radiation and its sensitivity to the crucial parameters still need to be investigated thoroughly. On the aspect of remote sensing application, the spatial pattern and temporal variations of surface radiation budgets are attractive issues and remain to be exploited further.

Under the unique physical settings and influenced by a fast urbanization process, the urban climate in Beijing has distinct features. In recent years, the adverse climatic effects caused by urbanization become prominent and harmful, for example, the intensity of UHI in Beijing is increasing with a rate of 0.31 K every 10 years [16]. This phenomenon has attracted the attention of ordinary people, academia and government. However, research about radiation budget in the Beijing metropolitan area is lacking. In this research, a practical approach was developed for calculating the surface net radiation by parameterizing the crucial factors such as the land surface emissivity, land surface temperature, surface shortwave broadband albedo, and longwave atmospheric counter radiation, based on the Landsat TM images and ancillary meteorological data. The spatial patterns and seasonal variations of surface radiation budget in the Beijing metropolitan area were investigated by comparisons between the urban and suburban areas from two Landsat TM images acquired in the summer and winter. The spatial patterns and seasonal variations of the land surface temperature, surface albedo, shortwave and longwave radiation fluxes were also discussed. The results will be useful for understanding the change rules of urbanization in the process of urban climate for such a mega-city.

2 STUDY AREA

The municipality of Beijing is located in northern China, from 39°26'N to 41°03'N and 115°25'E to 117°30'E, with mountains to the west, north and northeast of the city. This region is in the warm temperate zone and has annual average atmospheric temperatures of about 10.0-12.0°C. Beijing has distinct seasons, with a hot and humid summer and a cold and dry winter. As the capital and the second largest city in China, the municipality of Beijing has 18.953 million inhabitants, including 15.38 million permanent residents and 3.573 non-permanent natives. 63.25% of the total population lives in the core and the surrounding districts [17].

A region covering four downtown districts and four extended districts was selected as the study area (the blue rectangle in Fig. 1). Most of the terrain in the study area is flat, with the exception of hills located in the west and northwest. Commercial and business areas are concentrated in the central part of the study area, which is characterized by high-rise buildings and higher albedo materials. Low-rise houses covered by tiles made of lower albedo

materials are also dispersed throughout the city, but most are concentrated in the downtown districts.

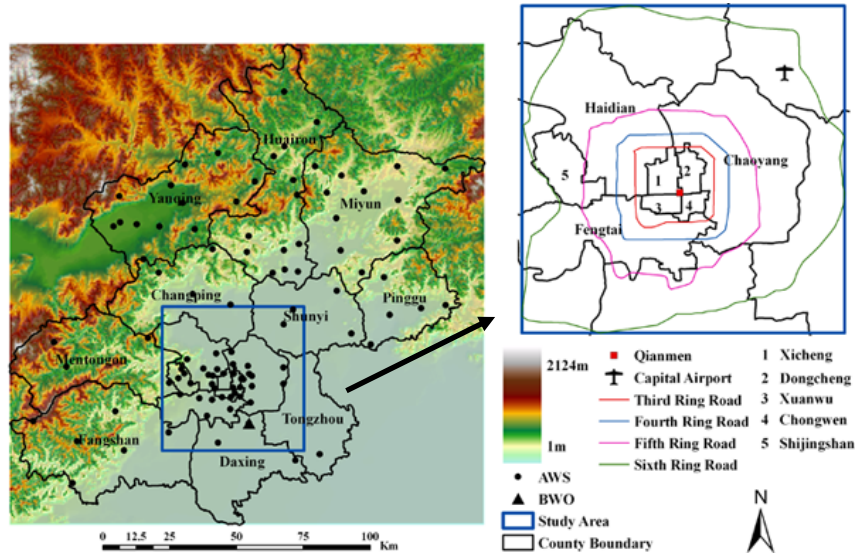


Fig. 1. Topographic map of Beijing. The digital elevation model (DEM) is shown in color. The automated weather stations (AWS) and Beijing Weather Observatory (BWO) are also shown in this figure.

3 DATA

3.1 Remote sensing images

In order to examine the spatial distribution of the radiation budget in the summer and winter, two Landsat-5 Thematic Mapper (TM) images, dated on July 6, 2004 and December 3, 2006, respectively, were used in this research. Both images were acquired under clear conditions. The images were purchased from the China Remote Sensing Satellite Ground Station (CRSSG), which corrected the radiometric and geometric distortions of the images to a quality level of 1G before delivery. The images were further geo-rectified to a Gauss-Kruger projection based on a rectified ASTER image through the second order polynomial method. During the geometric rectification, 55 ground control points (GCP) were selected for the 2004 image and 40 points for the 2006 image. Each image was resampled using the nearest neighbor algorithm with a pixel size of 30 m for all bands including the thermal band. The resultant root-mean-squared error was found to be 0.43 pixel for the 2004 image, and 0.48 pixel for the 2006 image.

Knowledge of land cover is essential for analyzing the surface radiation budget over different surfaces. In this research, each image was classified into seven types of land cover: forest, crop, bare soil, grassland, high-rise building surface, low-rise building surface and water (Fig. 2). For this classification we used the combined method of maximum-likelihood and visual interpretation. It should be noted that both high-rise building surface and low-rise building surface were identified through their color tones; the dry concrete, glass, and metal of the high-rise buildings are brighter and the tiles covering the one-two story houses in the downtown districts, as well as the asphalt and tar of the low-rise buildings are darker. 300 random samples were utilized to assess the classification accuracy, and it was found that the

resultant overall classification accuracy and kappa coefficient for the summer image were 83.67% and 0.7977, respectively; the overall classification accuracy and kappa coefficient for the winter image were 81.00% and 0.7434, respectively.

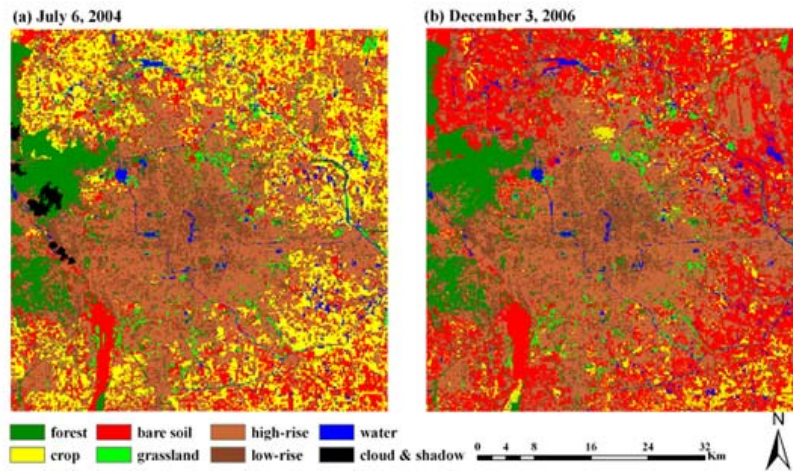


Fig. 2. Land cover maps of Beijing for July 6, 2004 and December 3, 2006. “High-rise” and “low-rise” denote high-rise and low-rise buildings, respectively.

3.2 Meteorological data

The meteorological data were acquired from the automated weather stations (AWSs) managed by the Beijing Meteorological Bureau (Fig. 1). There were 29 stations with atmospheric temperature and 15 stations with relative humidity records for July 6, 2004, and 39 stations with atmospheric temperature and 31 stations with relative humidity records for December 3, 2006. The average values of the parameters observed at 10:00 am and 11:00 am local time were used, because the Landsat-5 satellite passes over Beijing at approximately 10:30 am. In order to account for altitude of the weather stations where measurements were recorded, the average atmospheric temperature at each station was converted to the atmospheric temperature at sea level and then interpolated with the Inverse Distance Weighting (IDW) over the entire study area. Finally, the atmospheric temperature distribution near land surface was calculated from the temperature distribution at sea level and the digital elevation model (DEM) data, assuming 0.0065 K/m as the environment lapse rate [18]. IDW method was also utilized to interpolate the relative humidity with the same spatial resolution. The hourly-integrated total incoming solar radiation (MJ/m^2) (the sum of the direct solar radiation and the downward solar diffuse radiation at the ground surface) measured at the Beijing Weather Observatory ($39^{\circ}48'N$, $116^{\circ}28'E$) was converted to an average value for the entire hour (W/m^2), which was assumed constant for the entire study area.

4 METHODOLOGY

In order to calculate the net radiation, land surface parameters including albedo, land surface emissivity (LSE) and land surface temperature (LST) are required. The radiation fluxes contain the net radiation, the shortwave net radiation and the effective radiation, and the effective radiation is defined as the difference between the longwave surface emission and the longwave atmospheric counter radiation [2].

4.1 Radiometric calibration of Landsat-5 TM data

The following equation was used to convert the digital number (DN) of all bands into at-sensor spectral radiance [19]:

$$L_{\lambda} = G_{\text{rescale}} \times Q_{\text{cal}} + B_{\text{rescale}} \quad (1)$$

where L_{λ} is at-sensor spectral radiance in $\text{W}/(\text{m}^2 \cdot \text{sr} \cdot \mu\text{m})$; G_{rescale} and B_{rescale} are band-specific rescaling factors; Q_{cal} is the quantized calibrated pixel value in DNs.

The Second Simulation of the Satellite Signal in the Solar Spectrum (6S) model was applied for atmospheric correction. For the thermal band, at-sensor brightness temperature was calculated following the formula below [19]:

$$T_{\text{B}} = K_2 / \ln(K_1 / L_{\lambda} + 1) \quad (2)$$

where T_{B} is at-sensor brightness temperature in Kelvin and K_1 and K_2 are pre-launch calibration constants. For Landsat-5 TM, $K_1=607.76 \text{ W}/(\text{m}^2 \cdot \text{sr} \cdot \mu\text{m})$, and $K_2=1260.56 \text{ K}$.

4.2 Land surface parameters calculation

Land surface albedo is the integral value for the bio-directional reflectance distribution function (BRDF) at all view directions. It determines the proportion of the reflected solar radiation to the broadband shortwave irradiance in the range of 0.30-3.00 μm . The conversion formula proposed by Liang [20] was used in this study.

Land surface broadband emissivity is required to retrieve LST, but few methods have been developed to estimate the broadband emissivity from Landsat TM/ETM+ data. Considering the wide spectral range (10.40-12.50 μm) in the thermal infrared band of Landsat TM, we assumed the broadband emissivity was equal to the spectral emissivity of band 6 (S. Kato, personal communication, 18 October 2007). In this research, we calculated LSE based on the normalized difference vegetation index (NDVI) following [21-22].

If $\text{NDVI} < 0.20$ and a pixel was water, the emissivity was assigned as $\varepsilon_{\text{w}}=0.995$ [23]. Otherwise, the pixel was considered as bare surface with sparse to no vegetation, and equation (3) was adopted:

$$\varepsilon = 0.980 - 0.042\rho_3 \quad (3)$$

where ε is emissivity and ρ_3 is the surface reflectance in the red channel (TM band 3). The origin of this equation can be traced back to [24, 21-22].

If $\text{NDVI} > 0.50$, a pixel was considered fully vegetated, and the emissivity was assigned as $\varepsilon_{\text{v}}=0.990$ [21].

If $0.20 \leq \text{NDVI} \leq 0.50$, it may be assumed that a pixel was composed of vegetation, bare soil or urban surfaces. It was demonstrated the measured emissivity of an urban surface was approximately 0.972 in Beijing [25], which was similar to that of bare soil with a value of 0.973, simulated by [22]. Indeed, an error of 0.001 for emissivity would not induce any error in land surface temperature retrieval. Therefore, we assumed that 0.973 was an appropriate value of emissivity for both bare soil and urban surfaces. The emissivity for a mixed pixel was calculated as [22]:

$$\varepsilon = 0.004P_{\text{v}} + 0.986 \quad (4)$$

where P_{v} is the proportion of vegetation and can be calculated by the following equation [26].

$$P_v = [(NDVI - NDVI_{\min}) / (NDVI_{\max} - NDVI_{\min})]^2 \quad (5)$$

where $NDVI_{\max}=0.50$, and $NDVI_{\min}=0.20$.

LST is one of the most important parameters in land surface processes. The mono-window algorithm proposed by Qin *et al.* [27] is used to estimate the LST from Landsat TM data:

$$T_s = [a(1 - C - D) + (b(1 - C - D) + C + D)T_B - DT_a] / C \quad (6)$$

where T_s is LST in Kelvin; $a=-67.355351$; $b=0.458606$; T_a is the mean atmospheric temperature in Kelvin; T_B is at-sensor brightness temperature in Kelvin, which is defined in Section 4.1; $C=\varepsilon\tau$, $D=(1-\tau)[1+(1-\varepsilon)\tau]$, and τ is the total atmospheric transmissivity of the thermal band.

For different standard atmosphere, Qin *et al.* (2001) derived the simple linear regression for approximating T_a from the air temperature, T_0 , near the ground [27]. In this paper, the mid-latitude summer model was used for July 6, 2004 and the mid-latitude winter model for December 3, 2006. In addition, the atmospheric transmissivity can be calculated based on the atmospheric water vapor content.

4.3 Surface radiation budget estimation

The surface net radiation flux can be calculated by [2]:

$$R_n = E_s + E_l = R_s(1 - \alpha) + \varepsilon\varepsilon_a\sigma T_a^4 - \varepsilon\sigma T_s^4 \quad (7)$$

where R_n is the net radiation flux on the ground surface in W/m^2 ; E_s is the surface shortwave net radiation flux in W/m^2 ; E_l is the surface longwave net radiation flux in W/m^2 ; R_s is the total incoming radiation at the ground surface in W/m^2 ; α is the surface albedo; $\varepsilon_a\sigma T_a^4$ is the longwave atmospheric counter radiation (L_d) in W/m^2 ; $\varepsilon\sigma T_s^4$ is the longwave surface emission in W/m^2 ; and σ is the Stefan-Boltzmann constant, $\sigma=5.6696\times 10^{-8} W\cdot m^{-2}\cdot K^{-4}$. According to the definitions, the effective radiation, E_0 , is equal to $-E_l$. The atmospheric emissivity (ε_a) can be calculated based on the empirical equation between the water vapor pressure and atmospheric temperature [28].

5. RESULTS

5.1 Validation of the net radiation flux R_n

Following the methods above, the land surface parameters and the surface radiation parameters were calculated for the summer and winter images (Fig. 3, Fig. 4 and Fig. 5). The hourly-integrated net radiation fluxes measured at BWO between 10:00 am and 11:00 am local time on the two dates were converted to an average value for the entire hour (W/m^2) and were used to validate the estimated net radiation fluxes. The net radiation flux was measured with a net pyrriometer. For the 2004-7-6 image, the measured and estimated R_n are $619.4 W/m^2$ and $576.4 W/m^2$, respectively, indicating that the absolute error for R_n is $-43.0 W/m^2$ and the relative error is -6.94% in the summer. For the 2006-12-3 image, the measured and estimated R_n are $144.4 W/m^2$ and $162.1 W/m^2$, respectively, indicating that the absolute error for R_n is $17.7 W/m^2$ and the relative error is 12.26% in the winter. It can be concluded that the estimation of net radiation flux from Landsat TM images and meteorological data enable us to adequately analyze the spatial patterns and seasonal variations in the surface radiation budget for an urban environment.

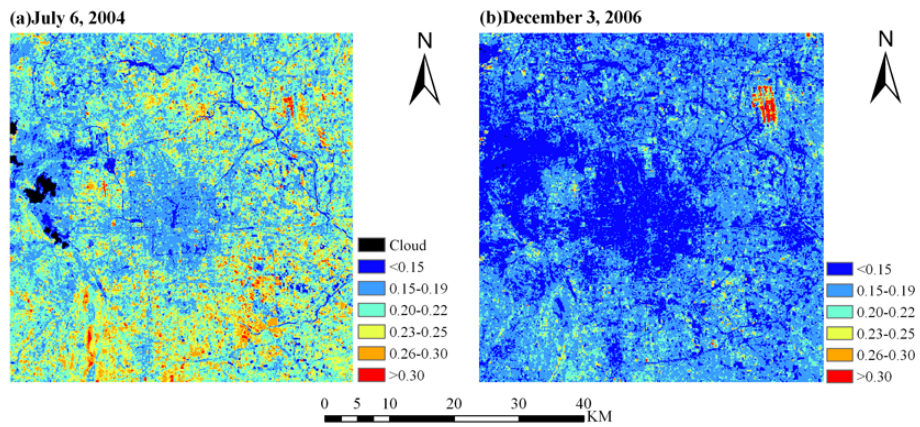


Fig. 3. Albedo in Beijing on July 6, 2004 and December 3, 2006. The black patches in (a) denote the masked-out clouds and their shadows.

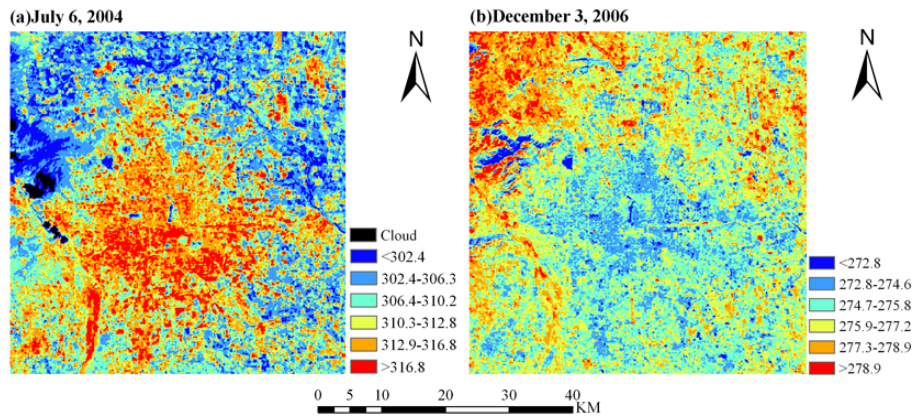


Fig. 4. Land surface temperature (in degrees Kelvin) in Beijing on July 6, 2004 and December 3, 2006. The black patches in (a) denote the masked-out clouds and their shadows.

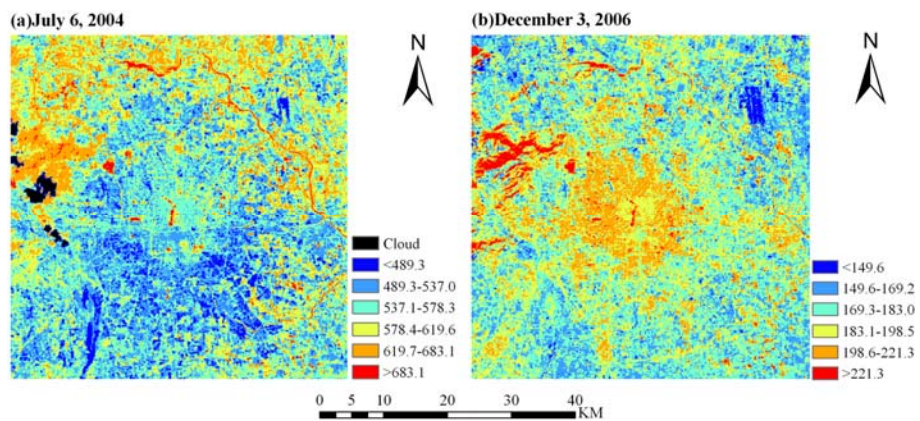


Fig. 5. Net radiation (in W/m^2) in Beijing on July 6, 2004 and December 3, 2006. The black patches in (a) denote the masked-out clouds and their shadows.

5.2 Sensitivity analysis of the net radiation flux R_n

The calculation of net radiation requires four parameters, albedo, LST, L_d and LSE. Sensitivity analysis can be employed to evaluate the impact of each of these parameters coupled with an estimation error on the total error in the estimating the net radiation flux, which is given by:

$$\delta R_n = R_n(x + \delta x) - R_n(x) \quad (8)$$

where x is one of the four parameters; δx is the estimated error for the variable x ; and $R_n(x)$ is the estimated net radiation.

Before discussing the sensitivity analysis, it is necessary to fully explain our experimental setup. The averaged values of albedo, LST, L_d and LSE were selected for the sensitivity analysis on each date. In the summer, the averaged values of these four parameters were 0.21, 309.8 K, 391.4 W/m² and 0.981, respectively. The range of albedo values was within 0.10-0.30, LST between 300.0-320.0 K, L_d 380.0-400.0 W/m², and LSE 0.975-0.995. In the winter, the average values of the four parameters were 0.16, 276.0 K, 193.7 W/m² and 0.977, and the range of values for these four parameters were 0.10-0.30, 270.0-290.0 K, 185.0-205.0 W/m² and 0.975-0.995. In order to satisfy the physical definition of LSE, only four errors on LSE were considered when analyzing the sensitivity, i.e., -2.0%, -1.0%, 1.0% and 2.0%.

It can be seen from Fig. 6 that R_n was slightly influenced by the errors for the albedo values. When the deviation in albedo was -2.0% to 2.0%, the estimated error for the net radiation flux, δR_n , was less than 5.2 W/m² in the summer and 2.3 W/m² in the winter. In addition, δR_n increased with the value of albedo. In contrast, LST exhibited a stronger influence on δR_n than albedo. As shown in Fig. 7, the error of R_n varied between 17.8.0 W/m² and 48.1 W/m² in the summer and 11.6 W/m² and 32.3 W/m² in the winter. Comparing with the two cases mentioned above, the absolute estimated error for R_n induced by L_d is moderate, and varied between 3.7 - 7.8 W/m² in the summer and 1.8 W/m² - 4.0 W/m² in the winter.

The deviation in LSE had minimal influence on δR_n , and its influence did not change with the value of LSE. In the summer, δR_n introduced by emissivity ranged from 1.3 W/m² to 2.6 W/m², indicating that R_n was rather sensitive to albedo. In contrast, R_n was more sensitive to emissivity than albedo in the winter.

The sensitivities of R_n to these parameters were also reflected by their respective impacts on the spatial distribution patterns of R_n . In order to quantitatively analyze the impact of each, their coefficient of variation (CV), which is defined as the ratio of standard deviation to the mean value, was used to investigate their spatial variations. Statistics for the whole study area suggest the CV of albedo was 20.1% in the summer and 27.9% in the winter and its spatial pattern was heterogeneous. Thus, $\pm 20.0\%$ error was selected to analyze the sensitivity of R_n to albedo. It can be seen from Fig. 6 that the spatial pattern of albedo significantly influenced the distribution of R_n . Similarly, although the CV values for LST were 1.7% in the summer and 0.6% in the winter, it has a significant influence on the spatial pattern of R_n . Moreover, LSE was stable over the study area, and its CVs were 1.0% in the summer and 0.7% in the winter. Therefore, it can be concluded that LSE had minimal influence on the spatial pattern of R_n . This is consistent with the conclusion in [14]. Thereby, more attention will be paid to both albedo and LST when analyzing the spatial pattern in the following sections, while L_d was not considered because the atmospheric state was very stable in limited spatial extent.

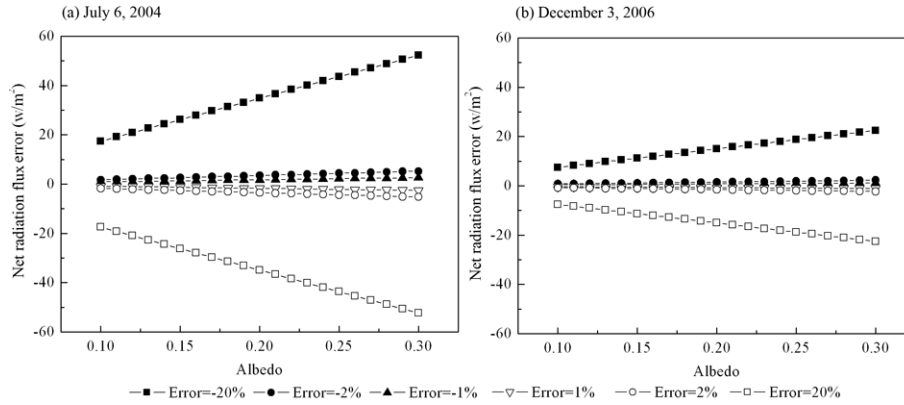


Fig. 6. The variation in surface net radiation flux error depending on the albedo error.

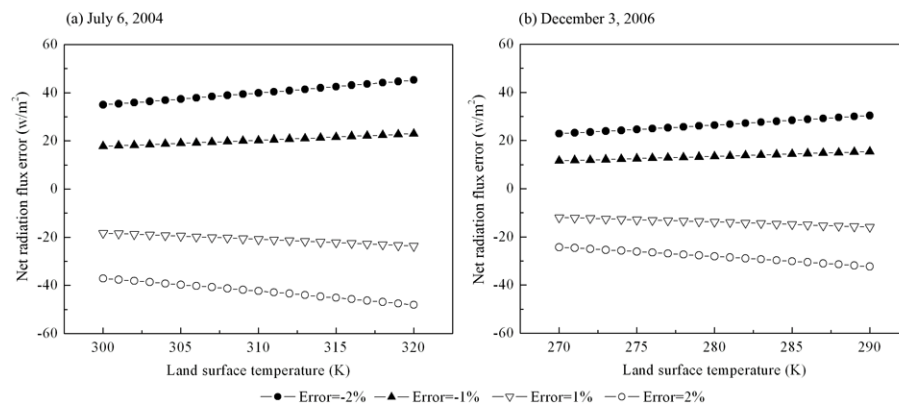


Fig. 7. The variation in surface net radiation flux error depending on the land surface temperature error.

5.3 Surface radiation budget by land cover type

5.3.1 In the summer

Fig. 3a shows the spatial distribution of albedo when the Landsat-5 satellite passed the region on July 6, 2004. It is apparent that the spatial pattern of albedo was concentric, i.e., albedo increased from the center of the city to the surrounding suburban areas. Low values of albedo around 0.15-0.19 can be detected within the Third Ring Road. In the south and northeast of the study area, there were many patches with higher albedo values of approximately 0.23-0.30, while in the northwest, albedo values were lower than 0.20, except for some bright patches.

The distribution of LST exhibited a remarkable UHI. The outline of the UHI is approximately the same as the boundary of the city, with the rural area (mainly comprised of crops) as the background (Fig. 4a). LST decreases systematically from the center of the city to the suburban area. It is interesting that the LST in the southern part of the city was higher than in the northern part. The areas with the highest UHI intensity were located near Qianmen and southeast of the Fourth Ring Road and Fengtai district. Higher LST also occurred in the wasteland and dry river bed of Yongding River of the southern suburban region of the study area and at the Capital Airport located in Shunyi County.

The net radiation exhibited a more complicated spatial distribution pattern (Fig. 5a). Net radiation also exhibited an obvious concentric pattern. The net radiation flux was ~ 537.1 - 578.3 W/m^2 within the Third Ring Road. Overall, the net radiation was less than 537.0 W/m^2 in the south part of the city between the Third Ring Road and the Sixth Ring Road. The north part of the city and the hilly areas in the northwest part of the study area had higher net radiation, which was ~ 578.4 - 683.1 W/m^2 . Water had an observed net radiation flux higher than 683.1 W/m^2 .

The mean and standard derivation of the net radiation, shortwave net radiation, effective radiation, LST and albedo were calculated according to the type of land cover. Table 1 shows the resultant statistics. Fig. 5a illustrates that reservoirs, lakes and pools were the "hot spots" of net radiation. Because of their low albedo and low temperature, the water in this study absorbed the largest amount of net radiation, with an average value of 694.2 W/m^2 . Water exhibited the highest shortwave radiation and the lowest effective radiation. Their standard derivation and CV were 61.0 W/m^2 and 8.8% , respectively. This indicates water presented the highest variations in net radiation. Moreover, the CVs for the shortwave net radiation and the effective radiation for water were 5.8% and 26.0% , respectively. Both were the highest values among all the types of land cover. This phenomenon may be the result of spectral alteration induced by an excessive number of aquatic plants in summer, which disturbs the albedo of water. Another potential cause is the alteration of the spectral response and thermal properties by pollution and temporary loblolly brought on by frequent rainstorms in the summer [27].

Vegetation, including grasslands, croplands and forests, exhibited yellow to orange tones (Fig. 5a), indicating the vegetation absorbed more net radiation than the built-up urban surfaces (i.e., high-rise and low-rise building surfaces) and bare soil, but less than water. This is important for the photosynthesis and the accumulation of dry matter. Vegetated areas, especially croplands, were cooler than urban surfaces, thus inducing less longwave emissions. The albedo of forested areas was similar to that of low-rise buildings. They absorbed approximately the same amount of shortwave net radiation in our study (about 715.0 W/m^2 to 713.5 W/m^2). However, croplands and grasslands were brighter than low-rise buildings, but darker than high-rise buildings, so these two types of vegetation absorbed more shortwave radiation than high-rise buildings. It should be noted that the radiation budgets of different vegetation types were different. Forested areas absorbed the largest amount of net radiation, grasslands the least, with croplands in between. These differences were caused by their different albedo and LST.

Bare soil was the brightest among all the types of land cover, because of its minimal absorption of shortwave net radiation (about 674.9 W/m^2 , about 4 W/m^2 lower than high-rise building). It was cooler than urban built-up surfaces, but hotter than the other natural surfaces (i.e., vegetation and water). As a result, bare soils absorbed the lowest amount of net radiation compared to the other types of land cover, except for high-rise buildings.

Urban built-up surfaces, including high-rise and low-rise buildings, exhibited higher LST than the other land cover types, as seen in Fig. 4a. The difference between the radiation budgets of different urban built-up surfaces was prominent. For example, due to the high albedo and temperature of high-rise buildings, their net radiation was ~ 54.9 W/m^2 lower than that of low-rise buildings. Most of the high-rise surfaces were rooftops, composed of concrete and glass, which have a high albedo and thus absorbed less shortwave net radiation. The LST of high-rise buildings was greatest among all the land cover types because of their considerable thermal capacity, which is the result of their large volumes and anthropogenic heat discharge from air-conditioners. In contrast, most of the low-rise surfaces were covered by tiles with low albedo, and absorbed more solar irradiance than the high-rise surfaces. There were also many trees planted around the low-rise residential houses, which had fewer air-conditioners than high-rise buildings for economic reasons. As a result, the temperature of

low-rise surfaces was about 5.4 K lower than that of high-rise surfaces. Accordingly, the effective radiation of low-rise surfaces was 19.9 W/m^2 less than that of high-rise surfaces.

Table 1. Statistics on the calculated radiation fluxes and land surface parameters for July 6, 2004.

| Land cover | Mean / Standard derivation | | | | |
|------------|----------------------------|--------------------------|--------------------------|-------------|-------------|
| | R_n (W/m^2) | E_s (W/m^2) | E_0 (W/m^2) | T_s (K) | α |
| Forest | 616.4 / 37.0 | 715.0 / 23.3 | 98.6 / 21.5 | 305.0 / 3.3 | 0.18 / 0.03 |
| Cropland | 597.0 / 34.5 | 692.2 / 27.9 | 95.2 / 16.3 | 304.0 / 2.6 | 0.21 / 0.03 |
| Bare soil | 540.1 / 45.8 | 674.9 / 29.4 | 134.9 / 26.4 | 310.8 / 4.0 | 0.23 / 0.03 |
| Grassland | 573.7 / 34.7 | 685.7 / 28.8 | 112.1 / 20.1 | 307.1 / 3.1 | 0.21 / 0.03 |
| High-rise | 520.2 / 36.3 | 678.7 / 32.1 | 158.3 / 25.4 | 316.2 / 3.7 | 0.22 / 0.04 |
| Low-rise | 575.1 / 33.5 | 713.5 / 26.3 | 138.4 / 27.3 | 310.8 / 4.1 | 0.18 / 0.03 |
| Water | 694.2 / 61.0 | 784.2 / 45.3 | 90.0 / 23.4 | 303.4 / 3.6 | 0.10 / 0.05 |

5.3.2 In the winter

Most of the surfaces exhibited blue and dark-blue tones in the winter, indicating overall lower albedo than in the summer (Fig. 3b). The low-albedo (lower than 0.15) regions were found within the Fourth Ring Road and in the hilly area in the northwest part of the study area. The medium-albedo (ranging from 0.15 to 0.22) regions were located in the areas surrounding the city. The Capital Airport exhibited the highest albedo value, which was greater than 0.30. The spatial pattern of LST in the winter was the inverse of the summer pattern (Fig. 4b). An urban cool island phenomenon occurred and the intensity of the cool island (the difference between the LST of urban surfaces and that of bare soil in the rural areas) was about 1.2 K. The northwest region revealed the highest surface temperatures.

The concentric pattern can be seen clearly in the distribution map of net radiation flux in the winter (Fig. 5b). The region within the Fourth Ring Road had a medium value of net radiation of $\sim 183.1\text{--}221.3 \text{ W/m}^2$. The values of net radiation for the regions located beyond the Fourth Ring Road decreased to less than 183.0 W/m^2 . Reservoirs, lakes and hilly areas absorbed the largest amount of net radiation, while the Capital Airport received the least.

Table 2 shows the resultant statistics according to the type of land cover. The analysis of net radiation by the type of land cover revealed the average value of net radiation in water was 213.6 W/m^2 , higher than the other types of land cover. The standard derivation and CV for water were 22.6 W/m^2 and 10.6%, respectively, indicating that the radiation budget for water was more heterogeneous than the others types of land cover. Water had the lowest mean albedo, but the highest CV (about 51.7%). This may be the result of the mixture of water and ice present in the winter. The effective radiation of water in the longwave region was lowest among all the types of land cover because water had the lowest temperatures.

Forests, croplands, and grasslands all exhibited a similar amount of effective radiation ($\sim 132.0 \text{ W/m}^2$), but a different amount of shortwave radiation. Croplands and grasslands absorbed a similar amount of solar irradiance, which was $\sim 19.0 \text{ W/m}^2$ lower than forests. This interesting phenomenon can be explained as follows. Most agricultural lands were converted to bare soil after harvest, leaving winter wheat as the dominating crop, which exhibited nearly the same spectral responses and thermal properties as the grasslands. As a result, croplands and grasslands obtained the same albedo and LST, inducing the equivalent amounts of the shortwave net radiation, effective radiation and net radiation. The LST of forested areas was slightly higher than that of croplands and grasslands, but the intrinsic spectral response and

large shadows in forests reduced the albedo of forests. As a result, forests received $\sim 19.0 \text{ W/m}^2$ more net radiation than the other two types of vegetated land cover.

Table 2. Statistics on the calculated radiation fluxes and land surface parameters for December 3, 2006.

| Land cover | Mean / Standard derivation | | | | |
|------------|------------------------------|------------------------------|------------------------------|-------------------|-------------|
| | $R_n \text{ (W/m}^2\text{)}$ | $E_s \text{ (W/m}^2\text{)}$ | $E_0 \text{ (W/m}^2\text{)}$ | $T_s \text{ (K)}$ | α |
| Forest | 200.0 / 28.7 | 332.1 / 20.6 | 132.0 / 11.6 | 276.0 / 2.5 | 0.11 / 0.05 |
| Cropland | 181.2 / 16.2 | 313.0 / 13.5 | 131.9 / 5.9 | 275.7 / 1.3 | 0.17 / 0.04 |
| Bare soil | 174.3 / 15.1 | 311.1 / 13.1 | 136.5 / 6.9 | 275.0 / 1.5 | 0.17 / 0.03 |
| Grassland | 180.4 / 16.1 | 311.8 / 14.2 | 131.4 / 5.3 | 275.7 / 1.2 | 0.17 / 0.04 |
| High-rise | 182.7 / 19.1 | 313.0 / 16.5 | 129.9 / 6.1 | 275.4 / 1.3 | 0.17 / 0.04 |
| Low-rise | 188.5 / 16.8 | 319.3 / 14.3 | 130.8 / 6.0 | 274.9 / 1.3 | 0.15 / 0.04 |
| Water | 213.6 / 22.6 | 338.7 / 18.7 | 125.2 / 8.5 | 273.9 / 1.8 | 0.10 / 0.05 |

Fig. 2b illustrates that of the types of land cover, bare soil was most abundant in the suburban areas in the winter, although there were some scattered wheat lands and golf courses. Bare soil absorbed the lowest net radiation, because it emitted the least shortwave irradiance and the most effective radiation of the different types of land.

A difference in radiation budgets between the low-rise building and high-rise building surfaces was present, but was not as significant as in the summer. The average albedo of low-rise surfaces was about 0.02 less than that of high-rise surfaces, and about differed by 6.3 W/m^2 in the amount of shortwave radiation absorbed. Since these two types of surfaces possessed the same LSTs and longwave radiation, the difference in net radiation fluxes was influenced largely by their difference in albedo. For all types of land cover, the ratio of effective radiation to shortwave net radiation increased in the winter, indicating that LST may play a less important role in the net radiation in the winter.

5.4 Seasonal variation in surface radiation budgets

The above analysis indicates that there were complicated seasonal variations in the radiation budgets and the primary factors that contributed to them (i.e., albedo and LST). Their magnitudes and spatial patterns in the summer and the winter were clearly different. Although there was a two-year interval between the acquisition dates of these images, no dramatic alternations in the type of land cover occurred, except for some minor expansion and rebuilding at the outskirts of the city. Here we examine the potential reasons for these distinct differences in the surface radiation budget for the summer and the winter if we ignore anthropogenic influences.

The seasonal variation of albedo, a primary parameter in land surface processes, was an important factor in contributing to the difference in the surface radiation budgets. From summer to winter, there were prominent decreases in albedo over all surfaces. While the albedo of water decreased about 4.2%, the albedo for other types of surfaces decreased by 18.4%~36.5%. The decrease in albedo for forested areas was the largest. Biological activities in vegetation decrease in winter, which may have resulted in the lower albedo for forests, grasslands, croplands and low-rise surfaces. In addition, albedo may have decreased in winter due to the lower solar elevation angle, which causes a greater number of shadows to be cast by high-rise buildings in the urban areas, trees and mountains.

The decrease of albedo enhanced the ability of surfaces to absorb the total incoming radiation. However, the amount of the incoming irradiance that reaches the ground decreases

dramatically in the winter, as determined by solar elevation angle (SEA). When the Landsat-5 satellite passed on July 6, 2004, SEA was 62.96° , and the total measured incoming radiation was 872.22 W/m^2 , while on December 3, 2006 the SEA decreased to 25.79° and the incoming radiation to 375.00 W/m^2 . It can be concluded that the changes in albedo and solar irradiance led to the change in surface radiation budgets, but the latter played a more important role. As a result, the total shortwave irradiance in the winter was only $\sim 53.6\text{-}56.8\%$ of the total shortwave irradiance in the summer.

Longwave emissions are controlled by LST. In the winter, the energy absorbed by land surfaces decreases significantly, thus LST decreases accordingly. The longwave emissions in the winter were only about $33.2\%\text{-}40.8\%$ of that in the summer. In particular, the longwave emissions of high-rise and low-rise surfaces decreased more dramatically, by 40.8% and 38.8% , respectively. Furthermore, the atmospheric counter radiation was 193.7 W/m^2 on December 3, 2006, about 49.5% of that on July 6, 2004, due to the cooler and drier atmosphere. As a result, effective radiation in the winter was greater than in the summer by $17.2\text{-}39.1\%$, for water, forested areas, croplands and grasslands. The effective radiation of bare soil was the same in both seasons. Because they were substantially cooler, the effective radiation of high-rise and low-rise buildings decreased by 18.0% and 5.5% , respectively in the winter.

A comparison between Fig. 5a and Fig. 5b suggests there were different patterns in net radiation in the summer and the winter. In the summer, croplands with active crops in suburban areas were brighter than low-rise building surfaces and absorbed less solar irradiance. Thus summer croplands were cooler than urban built-up surfaces because of their greater thermal inertia (in the range of $2000\text{-}3000 \text{ W}\cdot\text{s}^{1/2}\cdot\text{m}^{-2}\cdot\text{K}^{-1}$, according to [29]) and the higher evapotranspiration rate. The heating rate of urban built-up surfaces was greater than the suburban areas, because the evapotranspiration rate was low in the urban environment and the range of thermal inertia for urban surfaces were lower (in the range of $1400 \text{ W}\cdot\text{s}^{1/2}\cdot\text{m}^{-2}\cdot\text{K}^{-1}$ for concrete and $1300 \text{ W}\cdot\text{s}^{1/2}\cdot\text{m}^{-2}\cdot\text{K}^{-1}$ for brick, according to [30]). As a result, urban built-up surfaces absorbed less net radiation than the suburban areas, leading to the formation of a “basin” in net radiation (see Fig. 5). In the winter, bare lands in the countryside had a greater albedo and lower thermal inertia than the urban surfaces because of low water content and vegetation abundance [31]. The lower thermal inertia caused the bare lands heated rapidly after sunrise, and the cool island phenomenon occurred. The suburban areas absorbed less solar irradiance but had greater effective radiation, resulting in smaller net radiation. Therefore, the urban region of the city produced a “plateau” in the net radiation map in the winter.

6 DISCUSSIONS AND CONCLUSION

It is important to investigate radiation budgets over urban and suburban surfaces for urban climate research. In this paper, the applicability and feasibility of using Landsat-5 TM images in conjunction with meteorological data were investigated to estimate the surface radiation budgets in Beijing, China. Validation using *in situ* measurements suggests that estimating the net radiation with this method is sufficiently accurate. We conclude that satellite remote sensing can be used as an effective technique to improve modeling and analysis of the spatial patterns of surface energy balance for a mega-city such as Beijing.

The results suggest the net radiation in Beijing was controlled primarily by albedo and to a lesser degree by LST, while the influence of emissivity can be ignored. Different types of land cover exhibited different albedo and LST. Consequently they exhibited diverse radiation budgets, including the shortwave net radiation, the effective radiation and the net radiation. In particular, two types of urban built-up surfaces, i.e., high-rise and low-rise building surfaces, exhibited different albedo and LST. In the summer, the high-rise building surface had high albedo and high temperatures, which resulted in overall low shortwave net radiation and net

radiation. The low-rise building surfaces absorbed significant quantities of solar radiation and were cooler than the high-rise building surfaces, and thus exhibited higher net radiation than the high-rise building surface. In the winter, the difference in their radiation budgets was smaller.

The seasonal variations in the surface radiation budgets were also investigated. From summer to winter, the decrease in the shortwave net radiation and the net radiation were mainly controlled by the change of the solar elevation angle. In the winter, all land surfaces were darker, and their ability to absorb solar radiation was thus enhanced. Natural surfaces, including water and three types of vegetation, absorbed less longwave radiation in the winter, while the artificial surfaces including low-rise and high-rise buildings absorbed more because they were much cooler in the winter.

The main driving force of the Earth system is radiation forcing, and a detailed and quantitative knowledge of the Earth radiation field is crucial for understanding and predicting the evolution of the components of the Earth system [13]. However, the stations for measuring the surface radiation budget are still rare, especially in urban areas. Advents of satellite remote sensing provide the possibility to map the spatial-distributed surface radiation budget. Optical and thermal remote sensing images with relatively high spatial resolution are appropriate for calculating the surface radiation fluxes in urban and suburban areas. These calculations can obtain acceptable accuracies, as proven by our research. Based on these estimated radiation parameters, influences of urbanization on surface radiation budget can be modeled. Although our approach is proposed for Landsat TM data, it is feasible to extend this approach to other remote sensing data, such as Terra ASTER, Terra/Aqua MODIS and NOAA AVHRR, for acquiring in-depth knowledge on the spatial and temporal variations of surface radiation budget.

Acknowledgments

This work is supported by an Open Fund of State Key Laboratory of Remote Sensing Science, Jointly Sponsored by Beijing Normal University and the Institute of Remote Sensing Applications of Chinese Academy of Sciences. The assistance from Ma Wei of Beijing Normal University in pre-processing the data is acknowledged.

References

- [1] R. Pielke Sr, "Land use and climate change," *Science* **310**, 1625-1626 (2005) [doi: 10.1126/science.1120529].
- [2] P. Sheng, J. Mao, J. Li, A. Zhang, J. Sang and N. Pan, *Atmospheric Physics*, 1st ed., Peking University Press, Beijing (2003).
- [3] E. Hurtado and J. Sobrino, "Daily net radiation estimated from air temperature and NOAA-AVHRR data: A case study for the Iberian Peninsula," *Int. J. Rem. Sens.* **22**, 1521-1533 (2001) [doi: 10.1080/01431160152027638].
- [4] Y. Ma, "Remote sensing parameterization of regional net radiation over heterogeneous land surface of Tibetan Plateau and arid area," *Int. J. Rem. Sens.* **24**, 3137-3148 (2003) [doi: 10.1080/0143116021000021198].
- [5] G. Bisht, V. Venturini, S. Islam, and L. Jiang, "Estimation of the net radiation using MODIS (Moderate Resolution Imaging Spectroradiometer) data for clear sky days," *Rem. Sens. Environ.* **97**, 52-67 (2005) [doi: 10.1016/j.rse.2005.03.014].
- [6] G. Cai, Y. Xue, Y. Hu, J. Guo, Y. Wang, and S. Qi, "Quantitative study of net radiation from MODIS data in lower boundary layer in Poyang Lake area of Jiangxi Province, China," *Int. J. Rem. Sens.* **28**, 4381-4389 (2007) [doi:10.1080/01431160701244831].
- [7] T. Oke and R. Fuggle, "Comparison of urban/rural counter and net radiation at night," *Bound. Layer. Meteorol.* **2**, 290-308 (1972) [doi: 10.1007/BF02184771].

- [8] J. White, F. Eaton, and A. Auer Jr, "The net radiation budget of the St. Louis metropolitan area," *J. Appl. Meteorol.* **17**, 593-599 (1978) [doi: 10.1175/1520-0450(1978)017<0593:TNRBOT>2.0.CO;2].
- [9] T. Oke, "The urban energy balance," *Prog. Phys. Geog.* **12**, 471-508 (1988) [doi: 10.1177/030913338801200401].
- [10] T. Oke, R. Spronker-Smith, E. J. Áuregui, and C. Grimmond, "The energy balance of central Mexico City during the dry season," *Atmos. Environ.* **33**, 3919-3930 (1999) [doi: 10.1016/S1352-2310(99)00134-X].
- [11] K. Anandakumar, "A study on the partition of net radiation into heat fluxes on a dry asphalt surface," *Atmos. Environ.* **33**, 3911-3918 (1999) [doi: 10.1016/S1352-2310(99)00133-8].
- [12] A. Christen and R. Vogt, "Energy and radiation balance of a central European city," *Int. J. Climatol.* **24**, 1395-1421 (2004) [doi: 10.1002/joc.1074].
- [13] N. Chrysoulakis, "Estimation of the all-wave urban surface radiation balance by use of ASTER multispectral imagery and in situ spatial data," *J. Geophys. Res.* **108**, 4582 (2003) [doi: 10.1029/2003JD003396].
- [14] C. Frey, G. Rigo, and E. Parlow, "Urban radiation balance of two coastal cities in a hot and dry environment," *Int. J. Rem. Sens.* **28**, 2695-2712 (2007) [doi: 10.1080/01431160600993389].
- [15] G. Rigo and E. Parlow, "Modelling the ground heat flux of an urban area using remote sensing data," *Theor. Appl. Climatol.* **90**, 185-199 (2007) [doi: 10.1007/s00704-006-0279-8].
- [16] S. Yu, L. Bian, and X. Lin, "The relation between urbanization and the change of Beijing UHI," *Sci. China. Ser. D.* **35**, 97-106 (2005).
- [17] X. Yu, *Beijing Statistical Yearbook*; 1st ed., Chinese Statistics Press, Beijing (2003).
- [18] S. Kato and Y. Yamaguchi, "Analysis of urban heat-island effect using ASTER and ETM+ data: separation of anthropogenic heat discharge and natural heat radiation from sensible heat flux," *Rem. Sens. Environ.* **99**, 44-54 (2005) [doi: 10.1016/j.rse.2005.04.026].
- [19] G. Chander, B. Markham, and D. Helder, "Summary of current radiometric calibration coefficients for Landsat MSS, TM, ETM+, and EO-1 ALI sensors," *Rem. Sens. Environ.* **113**, 893-903 (2003) [doi: 10.1016/j.rse.2009.01.007].
- [20] S. Liang, "Narrowband to broadband conversions of land surface albedo: I. Algorithms," *Rem. Sens. Environ.* **76**, 213-238 (2001) [doi: 10.1016/S0034-4257(00)00205-4].
- [21] J. Sobrino, N. Raissouni, and Z. Li, "A comparative study of land surface emissivity retrieval from NOAA data," *Rem. Sens. Environ.* **75**, 256-266 (2001) [doi: 10.1016/S0034-4257(00)00171-1].
- [22] J. Sobrino, J. Jiménez-Muñoz, and L. Paolini, "Land surface temperature retrieval from Landsat TM 5," *Rem. Sens. Environ.* **90**, 434-440 (2004) [doi: 10.1016/j.rse.2004.02.003].
- [23] Z. Qin, W. Li, B. Xu, Z. Chen, and J. Liu, "The estimation of land surface emissivity for Landsat TM6," *Rem. Sens. Land Resources* **61**, 28-36 (2004).
- [24] J. Sobrino and N. Raissouni, "Toward remote sensing methods for land cover dynamic monitoring: application to Morocco," *Int. J. Rem. Sens.* **21**, 353-366 (2000) [doi:10.1080/014311600210876].
- [25] M. Huang, B. Chen, S. Liu, C. Cheng, and R. Peng, "An analysis of the city temperature abnormal area based on TM data," *Rem. Sens. Land Resources* **73**, 23-27 (2007).
- [26] T. Carlson and D. Ripley, "On the relation between NDVI, fractional vegetation cover, and leaf area index," *Rem. Sens. Environ.* **62**, 241- 252 (1997) [doi: 10.1016/S0034-4257(97)00104-1].

- [27] Z. Qin, A. Karnieli, and P. Berliner, "A mono-window algorithm for retrieving land surface temperature from Landsat TM data and its application to the Israel-Egypt border region," *Int. J. Rem. Sens.* **22**, 3719-3746 (2001) [doi: 10.1080/01431160010006971].
- [28] W. Brutsaert, *Evaporation into the Atmosphere-Theory, History, and Applications*, Reidel Publishing, Dordrecht, (1982).
- [29] J. Sobrino and M. El Kharraz, "Combining afternoon and morning NOAA satellites for thermal inertia estimation: 1. Algorithm and its testing with hydrologic atmospheric pilot experiment-sahel data," *J. Geophys. Res.* **104**, D8 (1999) [doi:10.1029/1998JD200109].
- [30] W. Carnahan and R. Larson, "An analysis of an urban heat sink," *Rem. Sens. Environ.* **33**, 65-71 (1990) [doi: 10.1016/0034-4257(90)90056-R].
- [31] K. Wang, J. Wang, P. Wang, M. Sparrow, J. Yang, and H. Chen, "Influences of urbanization on surface characteristics as derived from the moderate-resolution imaging spectroradiometer: a case study for the Beijing metropolitan area," *J. Geophys. Res.* **112**, D22S06 (2007) [doi: 10.1029/2006JD007997].